EES Solar

PAPER

View Article Online
View Journal | View Issue

Cite this: *EES Sol.*, 2026, **2**, 369

Bandgap-tunable transparent perovskite solar cells for 4T Si/perovskite tandem photovoltaics with PCE > 30% *via* rational interface management

Abhijit Singha, †[a] Tiankai Zhang, †[b] Ananta Paul, [c] M. M. Anas, [d] Karthik Raitani, [d] Manas Misra, [e] Subir Manna, [e] Vishnu Kumar, [e] Sudhanshu Mallick, [c] K. R. Balasubramaniam, [a] Pradeep R. Nair, *[d] Feng Gao *[b] and Dinesh Kabra *[e]

Silicon/perovskite tandem solar cells are predominantly recognized as a promising next-generation photovoltaic technology. The precise control of interfacial defects with appropriate energy level alignment between charge transport layers (CTLs) and the perovskite absorber is a crucial factor influencing the overall photovoltaic performance of perovskite solar cells (PSCs). This study investigates the substitution of conventional lithium bis(trifluoromethane)sulfonimide (LiTFSI)- and 4-*tert*-butylpyridine (t-BP)-doped spiro-MeOTAD with a post-oxidation-free, ion-modulated spiro-MeOTAD hole transport layer (HTL) for tunable bandgap transparent PSCs. The incorporation of 4-*tert*-butyl-1-methylpyridinium bis(trifluoromethanesulfonyl)imide ($TBMP^+TFSI^-$) enables reduced Shockley-Read-Hall (SRH) recombination and controlled work function tuning, leading to enhanced quasi-Fermi level splitting (QFLS). Three different perovskite compositions are employed, with perovskite 2 (1.61 eV) demonstrating optimal performance with both control and ion-modulated spiro-MeOTAD, resulting in minimal photovoltaic performance deviations. In contrast, perovskite 1 (1.52 eV) and perovskite 3 (1.72 eV) exhibit suboptimal optoelectronic properties with the control HTL. The $TBMP^+TFSI^-$-doped spiro-MeOTAD HTL enhances the photoluminescence quantum efficiency (PLQY) and carrier lifetime by reducing interfacial defects, improving the open circuit voltage (V_{OC}) and fill factor (FF), in agreement with our detailed simulation results. Integrating the optimized PSCs with an n-type tunnel oxide passivated contact (n-TOPCon) silicon (Si) solar cell in a 4-terminal (4T) tandem configuration achieves a power conversion efficiency (PCE) of 30.2%, highlighting the potential of ion-modulated spiro-MeOTAD for efficient and stable tandem solar cells.

Received 24th October 2025
Accepted 8th January 2026

DOI: 10.1039/d5el00175g

rsc.li/EESSolar

Broader context

Silicon/perovskite tandem solar cells represent an emerging pathway toward next-generation photovoltaics, yet interfacial defects and energy level mismatches between perovskite absorbers and charge transport layers (CTLs) critically limit their efficiency and stability. Conventional LiTFSI- and t-BP-doped spiro-MeOTAD hole transport layers (HTLs) require post-oxidation and exhibit poor ionic and environmental stability. Here, an ion-modulated, post-oxidation-free spiro-MeOTAD employing 4-*tert*-butyl-1-methylpyridinium bis(trifluoromethanesulfonyl)imide ($TBMP^+TFSI^-$) is introduced to achieve controlled work function tuning and effective interfacial defect passivation. This strategy suppresses non-radiative recombination, enhances quasi-Fermi level splitting, and improves the V_{OC} and fill factor across a range of perovskite band gaps. Integration of optimized transparent perovskite subcells with an n-TOPCon Si bottom cell in a 4-terminal configuration delivers a power conversion efficiency of 30.2%. These findings establish ion-modulated spiro-MeOTAD as a robust, scalable HTL design for high-efficiency and durable perovskite/silicon tandem photovoltaics.

Introduction

The discovery of hybrid organic and inorganic lead halide perovskites as photo-absorber materials has ushered in a ground-breaking era in photovoltaic (PV) technology. They exhibit exceptional optoelectronic properties, enabling near-theoretical power conversion efficiency (PCE) while significantly reducing fabrication costs compared to conventional monocrystalline silicon (Si) photovoltaics.[1–6] Moreover, beyond

[a]*Department of Energy Science and Engineering, Indian Institute of Technology Bombay, Mumbai, 400076, India*
[b]*Department of Physics, Chemistry and Biology (IFM), Linkoping University, Linkoping, 58183, Sweden. E-mail: feng.gao@liu.se*
[c]*Department of Metallurgical Engineering and Material Science, Indian Institute of Technology Bombay, Mumbai, 400076, India*
[d]*Department of Electrical Engineering, Indian Institute of Technology Bombay, Powai, Mumbai 400076, India. E-mail: prnair@ee.iitb.ac.in*
[e]*Department of Physics, Indian Institute of Technology Bombay, Powai, Mumbai 400076, India. E-mail: dkabra@iitb.ac.in*
† Contributed equally to this work.

standalone applications, perovskites have also facilitated the development of tandem or multijunction solar cells. This offers a pathway to surpass the efficiency limits of single-junction devices, particularly for terrestrial applications, owing to their advantageous photovoltaic properties and exceptional bandgap tunability.[7–12] The facile and efficient tunability of the bandgap, combined with their superior light absorption characteristics, makes perovskite solar cells (PSCs) highly suitable for integration into tandem configurations, enabling higher PCEs than single-junction solar cells.[13–15] Notably, the achievement of 32.5% and 33.7% efficiency in two-terminal (2T) Si/perovskite tandem solar cells by academic institutions, along with a 34.9% efficiency reported by industrial laboratories, underscores the transformative potential of this technology for the commercialization of tandem solar cells in terrestrial applications.[13,16–19] Si/perovskite 2T tandem solar cells represent a promising and transformative advancement in PV technology. However, a significant challenge hindering their commercialization is the considerable disparity in operational lifetimes between Si and perovskite subcells. In this context, four-terminal (4T) tandem solar cells offer a commercially viable alternative by providing greater flexibility.[20,21] Specifically, in the event of perovskite sub-cell degradation, replacement is feasible without compromising the overall operational lifespan of the tandem configuration, thereby enhancing long-term stability and reliability at a fraction of the overall levelized cost of electricity (LCOE).[22,23]

Bandgap-tunable PSCs are essential components of tandem solar cells, where a perovskite offers exceptional bandgap tunability with outstanding efficiency. However, a key observation in these solar cells is that an increase in the bandgap is accompanied by a roughly linear decrease in the current density. The expected improvement in the open-circuit voltage (V_{OC}) does not scale proportionally, leading to a reduction in the overall PCE.[24] This discrepancy arises from an increase in defect densities at higher bandgap perovskites as well as shifted energy levels, which jointly lower the PV performance by introducing additional non-radiative recombination pathways.[25] Transparent PSCs are essential for the development of tandem solar cells, as they enable efficient light transmission to the bottom sub-cell.[26] In these devices, the conventional opaque metal electrode is replaced with a transparent electrode, allowing photons beyond the perovskite band edge to be utilized by the underlying absorber.[27] Transparent PSCs are typically fabricated in either a negative–intrinsic–positive (n–i–p) or positive–intrinsic–negative (p–i–n) configuration. While the p–i–n architecture is the preferred choice for 2T Si/perovskite tandem solar cells due to reduced parasitic absorption in charge transport layers (CTLs), particularly because incident light enters from the thinner electron transport layer (ETL) side, its counterpart, the n–i–p structure, is better suited for 4T tandem configurations.[28] The n–i–p design benefits from the use of stable inorganic ETLs and mitigates the parasitic absorption losses associated with the commonly used spiro-MeOTAD hole transport layer (HTL), as light enters from the ETL/perovskite interface.[29] Moreover, a given set of traditional CTLs is typically optimized for a specific perovskite bandgap value. Any variation in the perovskite bandgap can lead to energy level misalignment at the CTL/perovskite interface, specifically at the HTL/perovskite interface.[30] This misalignment is more pronounced at the HTL/perovskite junction, as the valence band of the perovskite is predominantly influenced by halide orbitals, making it highly sensitive to changes in halide composition.[31,32] This misalignment induces band offsets, thereby lowering the implied open-circuit voltage (iV_{OC}) and ultimately reducing device efficiency.[30] To address these challenges, researchers have investigated various strategies, including (i) the incorporation of interfacial layers between CTLs and the perovskite absorber to mitigate band misalignment, (ii) the selection of CTLs with appropriate band alignment, and (iii) bulk perovskite modulation to achieve efficient band alignment. For instance, Caprioglio *et al.* systematically quantified the impact of misaligned CTLs on the V_{OC} and overall device efficiency. Their study demonstrated that integrating low-dimensional perovskites as interfacial passivation layers effectively reduces the band offset, thereby enhancing V_{OC}, particularly in wide bandgap (1.8 eV) perovskite absorbers.[25] Furthermore, Wang *et al.* incorporated alkylammonium bromide-based interfacial layers with varying chain lengths to form a 2D/3D heterostructure, achieving a maximum V_{OC} of 1.31 V in a triple-cation mixed-halide perovskite with a bandgap of 1.72 eV.[33] Additionally, Jaysankar *et al.* demonstrated that the incorporation of an atomic layer deposition (ALD)-derived Al_2O_3 passivation layer reduced the V_{OC} deficit, resulting in a 27.1% efficient 4-terminal (4T) Si/perovskite tandem solar cell.[34]

Beyond these approaches, several studies have also focused on modifying or incorporating different HTLs to mitigate V_{OC} loss. For example, Zhao *et al.* employed phosphorus-modulated NiO as an HTL in p–i–n PSCs, achieving a mere 24.69% relative V_{OC} loss and developing an all-perovskite, 2T monolithic tandem solar cell with a PCE of 27.66%.[35] Similarly, Wei *et al.* demonstrated that the incorporation of a bromine-substituted self-assembled monolayer (SAM)-based HTL enabled the device to reach 90% of the Shockley–Queisser (S–Q) V_{OC} limit for a 1.79 eV bandgap perovskite.[36] In addition to interfacial engineering, bulk perovskite modulation has also been investigated as a strategy to enhance V_{OC}. For example, Zhao *et al.* reported that the incorporation of phenethyl ammonium chloride (PMACl) resulted in a decrease of the V_{OC} deficit to 0.418 V.[37] Collectively, these studies underscore the importance of optimizing band alignment in bandgap-tunable PSCs to minimize V_{OC} deficits and ultimately achieve higher PCEs.

The inherent instability of PSCs hinders their commercial field deployment.[38–40] Notably, besides perovskites, commonly used CTLs also degrade over time.[41,42] Regular n–i–p PSCs typically employ doped spiro-MeOTAD HTLs, which, despite enabling high performance, require doping and oxidation for optimal conductivity and work function. Conventional spiro-MeOTAD doping with lithium bis(trifluoromethane)sulfonimide (LiTFSI) and 4-*tert*-butylpyridine (t-BP) involves an oxidation process lasting 10–24 hours, generating oxidized spiro-MeOTAD$\cdot$+$TFSI^-$ radicals and ensuring uniform morphology.[43] Moreover, residual dopants and by-products (*e.g.* Li_xO_y) form

during this process. Additionally, LiTFSI's hygroscopic nature leads to moisture absorption, converting it into bis(trifluoromethanesulfonyl)amine (HTFSI), which exacerbates water uptake.[44] These factors collectively compromise the stability of the HTL and eventually lead to device failure. Additionally, FK209 is commonly utilized to enhance the conductivity of conventional spiro-OMeTAD-based HTLs. However, it is important to note that the formation of oxidized spiro-OMeTAD radical species typically requires substantial amounts of LiTFSI and t-BP. Literature reports indicate that approximately 56 mol% of LiTFSI and 330 mol% of t-BP are required to produce only 10 mol% of oxidized spiro-OMeTAD radicals.[45] This high level of doping leads to the generation of undesirable by-products, highly sensitive to both moisture and thermal stress.[46] Although FK209 can slightly improve the oxidation efficiency of spiro-OMeTAD, it still necessitates the use of high concentrations of volatile t-BP, thereby contributing further to degradation-prone by-product formation and ultimately limiting overall device stability.[47]

To address these issues, a recently developed ion-modulated radical-doped spiro-MeOTAD HTL realizes optimal work function tuning through 4-*tert*-butyl-1-methylpyridinium bis(trifluoromethanesulfonyl)imide (TBMPTFSI) salt modulation with improved stability.[48] Compared to energy level optimization by chemical structure engineering of HTL molecules, the ion-modulated radical-doped spiro-MeOTAD HTL provides a more facile and controllable strategy to align the energy levels with reduced interfacial defects to wide bandgap perovskites.

In this study, we incorporated TBMPTFSI-tuned ion-modulated spiro-MeOTAD HTLs (Ion-Spiro) into the development of transparent PSCs with variable band gaps (1.52 eV, 1.61 eV, and 1.72 eV). For perovskite 2 (1.61 eV), the incorporation of Ion-Spiro results in negligible changes in photovoltaic performance, attributed to the minimal deviation of interfacial defects at the perovskite/HTL interface. In contrast, in narrow bandgap perovskites (1.52 eV), the incorporation of ion-modulated spiro-MeOTAD with precise tuning of the TBMPTFSI doping concentration resulted in ~50 mV enhancement in the V_{OC} (1.08 V → 1.13 V). This enhancement in V_{OC} resulted in a PCE of 21.3%, whereas the control device exhibited a maximum PCE of only 18.2%. Similarly, perovskite 3 (1.72 eV) also showed notable improvement (~20 mV) in V_{OC} while incorporating TBMPTFSI-tuned ion-modulated spiro-MeOTAD HTL. Optical analysis confirms that the reduction in the Shockley-Read-Hall (SRH) recombination constant achieved through Ion-Spiro incorporation suppressed interfacial defects and optimized energy level alignment, thereby enhancing the photoluminescence quantum yield (PLQY), quasi-Fermi level splitting (QFLS), and ultimately iV_{OC}. Moreover, these transparent PSCs are integrated with n-type tunnel oxide passivated contact (n-TOPCon) monocrystalline Si solar cells in a 4T tandem configuration and achieved 30.2% efficiency. Therefore, this study demonstrates that the incorporation of an ion-modulated spiro-MeOTAD HTL provides an effective strategy for controlling interfacial defects and energy level tuning, thereby facilitating highly efficient and stable transparent PSCs for the development of Si/perovskite tandem solar cells with PCEs exceeding 30%.

Results

Precise control over the band alignment between the perovskite photo-absorber and CTLs is crucial for reducing interfacial defects and consequently achieving higher photovoltage and enhanced PCE.[25] In this study, we investigate the incorporation of conventional doped spiro-MeOTAD and ion-modulated spiro-MeOTAD as HTLs in variable bandgap transparent PSCs. This study uses three different perovskites with varying A-cation and halide compositions (details are in the SI), which are denoted as perovskite 1 (~1.52 eV), perovskite 2 (~1.61 eV), and perovskite 3 (~1.72 eV). It is to be noted that the perovskite compositions used for this study are optimal for their respective band gaps (E_g) as per the reported literature.[49–51]

Fig. 1(a) illustrates the energy level alignment of perovskite materials with variable band gaps, along with control and TBMPTFSI salt-modified Ion-Spiro samples, as determined by ultraviolet photoelectron spectroscopy (UPS) in an n–i–p configured device architecture. With the increase in perovskite band gap, the valence band maximum (VBM) shifts gradually downward. Similarly, increasing the TBMPTFSI salt

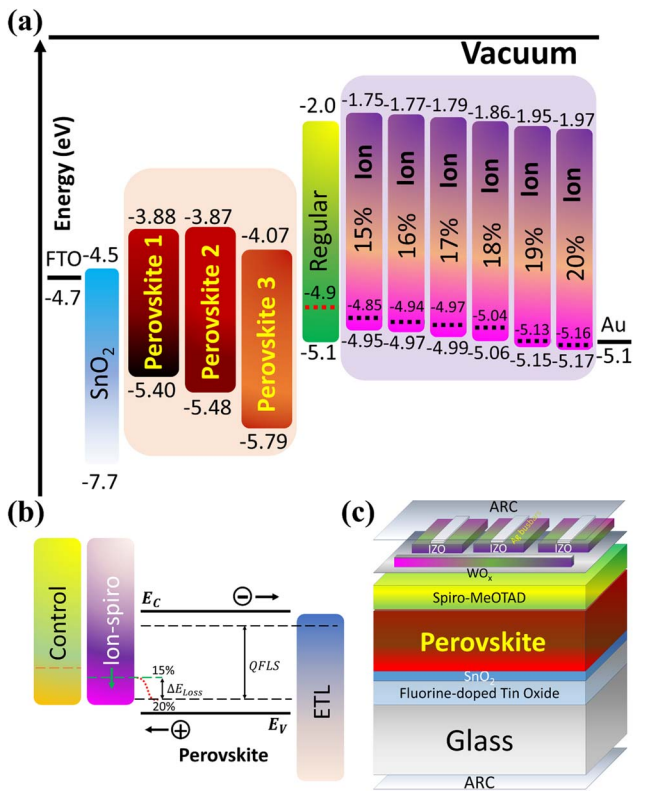

Fig. 1 Role of energy level tuning with the ion-modulated spiro-MeOTAD HTL. (a) Energy level diagram of the bandgap tuneable perovskites with the control and tuneable HOMO based Ion-Spiro, (b) schematic representation of work function tuning through TBMPTFSI salt concentration for perovskites, and (c) stacked device architecture of the transparent PSCs.

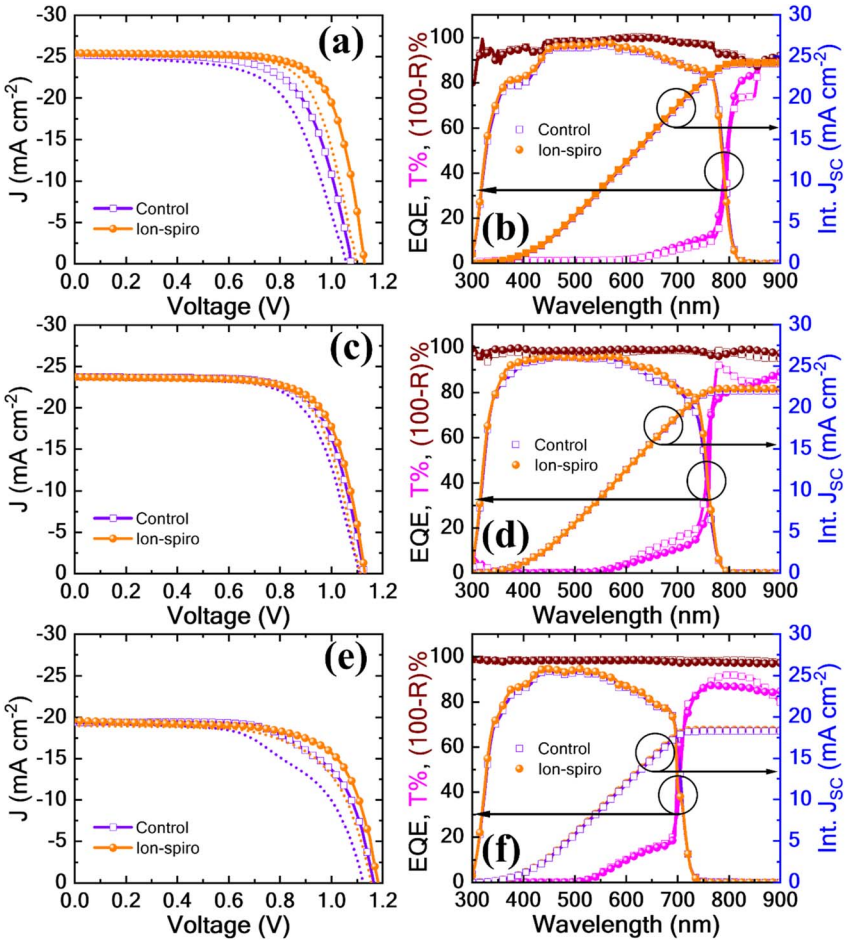

Fig. 2 Photovoltaic characteristics of the bandgap varying transparent PSCs with the control and ion-modulated spiro-MeOTAD HTL. (a, c, and e) Light $J-V$ characteristics with forward (dotted line) and reverse (solid line with symbols) scanning of the control (violet) and Ion-Spiro (orange) HTL-based transparent PSCs with perovskite 1, 2, and 3, respectively. (b, d, and f) EQE with integrated J_{SC}, transmission (pink), and 100-reflection (brown) of control (violet) and Ion-Spiro (orange) HTL-based transparent PSCs with perovskite 1, 2, and 3, respectively.

concentration in the Ion-Spiro hole transport layer (HTL) leads to a deeper HOMO level and a downward shift of its Fermi level. These concurrent shifts in the perovskite VBM and the Ion-Spiro HOMO enable controlled tuning of the interfacial energy level alignment. The fitted UPS spectra used for this analysis are presented in Fig. S1. The TBMPTFSI concentration is optimized within the range of 15–20% to achieve a favourable alignment with the corresponding perovskite energy levels, as discussed in detail in the subsequent sections. Additionally, conductive atomic force microscopy (C-AFM) measurements of the work function of the ion-modified spiro-MeOTAD films exhibit good agreement with the UPS results. The corresponding variations in the contact potential difference (V_{CPD}), reflecting the work function changes, are shown in Fig. S2. Fig. S3 compares the absorption spectra of oxidized conventional spiro-MeOTAD with the non-oxidized ion-modulated spiro-MeOTAD, revealing that the Ion-Spiro retains optical properties closely matching those of the oxidized counterpart.

The achievable quasi-Fermi level splitting (QFLS) is primarily governed by the combined effects of the interfacial energy level offset and defect states present in the control *vs.* Ion-Spiro, as schematically illustrated in Fig. 1(b). Notably, interfacial defect states may induce Fermi level pinning, diminishing the impact of engineered band alignment. In such cases, the attainable QFLS becomes largely dominated by interfacial defect densities, which will be discussed in detail in a later section of this manuscript.

The stacked device architecture of the transparent PSCs employed in this study is illustrated in Fig. 1(c). The architecture comprises a bilayer SnO_2 ETL, followed by perovskites with variable band gaps, and subsequently either conventional or ion-modulated spiro-MeOTAD as the HTL. An ultra-thin WO_3 buffer layer is incorporated to mitigate sputter-induced damage, followed by an RF-deposited indium zinc oxide (IZO) layer serving as the top transparent electrode (TE), with additional silver (Ag) metal grids. The optimization of the TEs is discussed in a separate study.[52–54]

The current–voltage ($J-V$) characteristics of the bandgap-tunable transparent PSCs with both control and ion-modulated spiro-MeOTAD HTLs are shown in Fig. 2a, c, and e. Fig. 2(a) illustrates the $J-V$ characteristics of the transparent PSCs incorporating perovskite 1. The control device exhibits

Table 1 Light $J-V$ parameters of the bandgap varying transparent PSCs with the control and ion-modulated spiro-MeOTAD HTL

Device	HTL	Scan direction	J_{SC}(mA cm^{-2})	V_{OC} (V)	FF (%)	PCE (%)	Int. J_{SC}(mA cm^{-2})
Perovskite 1	Control	RS	25.17	1.08	66.9	18.2	24.07
		FS	24.97	1.07	62.1	16.6	
	Ion-Spiro	RS	25.39	1.13	73.8	21.3	24.22
		FS	25.31	1.10	70.7	19.7	
Perovskite 2	Control	RS	23.57	1.13	71.6	19.1	22.1
		FS	23.45	1.11	68.4	17.8	
	Ion-Spiro	RS	23.70	1.13	72.5	19.4	22.3
		FS	23.66	1.12	70.9	18.8	
Perovskite 3	Control	RS	19.30	1.17	63.9	14.4	18.3
		FS	19.36	1.13	55.9	12.2	
	Ion-Spiro	RS	19.60	1.19	68.4	16.1	18.5
		FS	18.97	1.16	64.9	14.2	

a maximum PCE of 18.2% with a V_{OC} of 1.08 V, a short-circuit current density (J_{SC}) of 25.17 mA cm^{-2}, and a fill factor (FF) of 66.9%. In contrast, the ion-modulated spiro-MeOTAD HTL-based device demonstrates an enhancement of ~50 mV in V_{OC}, corroborating the optical analysis, resulting in a maximum V_{OC} of 1.13 V. Additionally, slight improvements in J_{SC} and FF to 25.39 mA cm^{-2} and 73.8%, respectively, contribute to a maximum PCE of 21.3%. The external quantum efficiency (EQE) analysis, along with reflection, transmission, and integrated J_{SC} data, is displayed in Fig. 2(b). Both devices exhibit a similar trend in the EQE spectrum; however, a distinct transmission spectrum is evident. Furthermore, the integrated J_{SC} values align well with the light $J-V$ analysis. Fig. 2(c) presents the light $J-V$ analysis of transparent PSCs incorporating perovskite 2. In contrast to perovskite 1, perovskite 2 exhibits no significant variation in V_{OC}. The control device achieves a maximum PCE of 19.1%, with V_{OC}, J_{SC}, and FF values of 1.13 V, 23.57 mA cm^{-2}, and 71.6%, respectively. Conversely, the ion-modulated spiro-MeOTAD-based device achieves a maximum PCE of 19.4%, with V_{OC}, J_{SC}, and FF values of 1.13 V, 23.70 mA cm^{-2}, and 72.5%, respectively. Fig. 2(d) illustrates the EQE spectrum along with transmission, reflection, and integrated J_{SC} data. Similar to perovskite 1, no significant differences are observed in the EQE and reflection spectra; however, distinct interference fringes are evident in the transmission spectrum. Fig. 2(e) depicts the $J-V$ analysis of transparent PSCs with perovskite 3. As for perovskite 1, a significant change in V_{OC} is noted. The control device exhibits a maximum PCE of 14.4%, with a maximum V_{OC} of 1.17 V, J_{SC} of 19.30 mA cm^{-2}, and an FF of 63.9%. In contrast, the ion-modulated spiro-MeOTAD-based device achieves the highest PCE of 16.1%, with a maximum V_{OC} of 1.19 V, J_{SC} of 19.60 mA cm^{-2}, and an FF of 68.4%. Fig. 2(f) presents the EQE spectrum alongside reflection, transmission, and integrated J_{SC} data. Similar to previous studies, no significant changes in the EQE spectrum and reflection characteristics are observed. However, both devices exhibit distinct interference fringes, resulting in a differentiated transmission spectrum. The integrated J_{SC} values of the devices are well aligned with the light $J-V$ analysis. All the PV parameters are tabulated in Table 1. It is important to note that all $J-V$ parameters mentioned above correspond to the optimal concentration of TBMPTFSI salt. The effect of the energy level alignment and reduced interfacial defects is also evident from the built-in-potential (V_{bi}) analysis from the dark $J-V$ characteristics of the champion transparent PSCs, as shown in Fig. S4.

The optimization of ion-modulated spiro-MeOTAD for perovskites with various bandgaps is performed by tuning the TBMPTFSI salt concentration. Herein, for perovskite 1, the salt concentration is varied from 15% to 17%, and the highest V_{OC} and FF, leading to the maximum PCE, are observed at 16% doping, as shown in Fig. S5. In addition to doping concentration, the spin-coating speed of the HTL also plays a crucial role, as the deposition process of ion-modulated spiro-MeOTAD differs from that of conventional spiro-MeOTAD. As the wettability and surface roughness of the perovskite surface vary with its composition, it is important to establish an optimal Ion-Spiro thickness, which in turn necessitates thickness optimization through spin speed variation. To optimize this parameter, the spin speed is varied from 4000 rpm to 6000 rpm in increments of 1000 rpm, while maintaining the TBMPTFSI doping concentration at 16%. The results indicate that for perovskite 1, an optimal spin speed of 5000 rpm yields the highest PCE, as illustrated in Fig. S6. Similarly, for perovskite 2, the doping concentration is varied from 16% to 19%, with the best performance observed at 17% doping, as shown in Fig. S7. Further spin speed optimization reveals that 3000 rpm is the most effective for perovskite 2, as depicted in Fig. S8. Moreover, the salt concentration and film thickness were also optimized for perovskite 3. In this case, the salt concentration was varied from 18% to 20%, while the spin speed was adjusted between 3000 rpm and 5000 rpm, as shown in Fig. S9 and S10, respectively. It was determined that a salt concentration of 19% combined with a spin speed of 4000 rpm provided the highest PCE for perovskite 3. Notably, with increasing salt concentration, along with work function modulation, an increase in spiro-radical concentration (SI – Experimental section) occurs, leading to enhanced conductivity, which has been reported elsewhere.[48]

The enhancement in V_{OC} likely arises from improved energy level alignment driven by Fermi level shifting, and/or a significant reduction in interfacial defect states. Previous studies suggest that changes in the HTL Fermi level generally do not

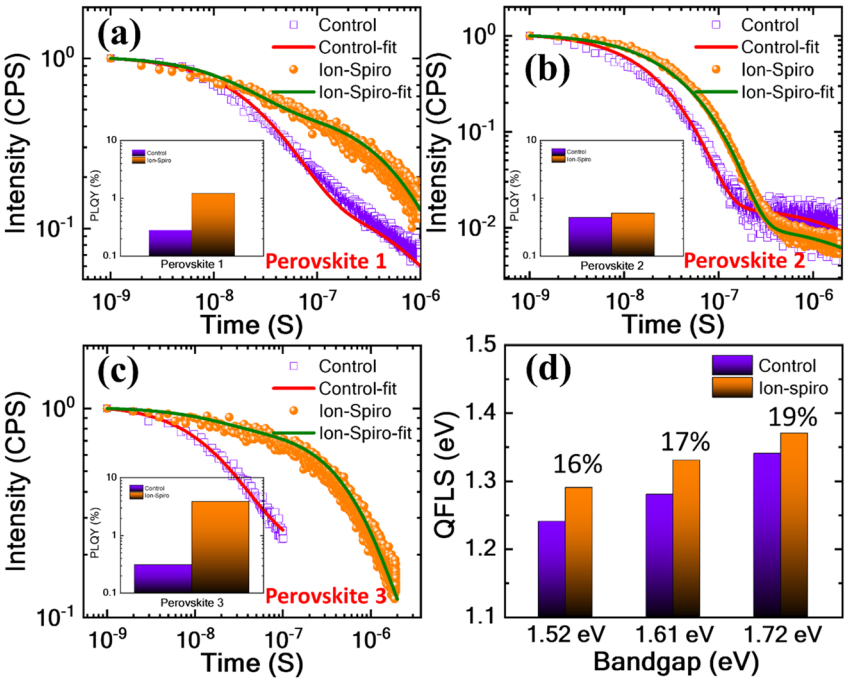

Fig. 3 Optical analysis of the bandgap varying transparent semi-processed PSCs (glass/FTO/SnO_2/perovskite/control or Ion-Spiro HTL) with control and ion-modulated spiro-MeOTAD HTL. Fitted TCSPC carrier lifetime decay with PLQY (inset) of (a) perovskite 1, (b) perovskite 2, and (c) perovskite 3. (d) Estimated QFLS of variable bandgap transparent PSCs with the control and ion-modulated spiro-MeOTAD HTL.

strongly affect the V_{OC} because mobile ionic defects (*e.g.* iodine vacancies) in the perovskite can migrate and accumulate at the perovskite/HTL interface.[55] These ions form thin Debye layers that effectively compensate for the potential differences caused by different HTM work functions. As a result, the perovskite layer self-adjusts, making the V_{OC} largely insensitive to the HTL work function.

Thus, to gain a comprehensive understanding of the impact on Ion-Spiro, specifically, whether it is attributable solely to the energy level mismatch or predominantly to interfacial defects, we performed a detailed analysis of the recombination dynamics based on carrier lifetime measurements (Note 1, SI). The fitted time-correlated single photon counting (TCSPC) spectra of all three perovskites with optimized salt concentration for Ion-Spiro HTL-based samples are shown in Fig. 3a, b, and c, respectively. In agreement with J–V studies, the average carrier lifetime exhibited minimal variation for perovskite 2, which is shown in Fig. 3(b). The control samples of perovskite 2 showed a maximum average carrier lifetime of 34.75 ns, whereas the ion-modulated spiro-MeOTAD samples exhibited an enhanced carrier lifetime of 53.49 ns. Moreover, there is a substantial difference in carrier lifetime observed for perovskites 1 and 3 due to a higher density of interfacial defects. Specifically, perovskite 1 exhibited carrier lifetimes of 318.79 ns and 589.76 ns for control and ion-modulated spiro-MeOTAD samples, respectively, as shown in Fig. 3(a). Furthermore, Fig. 3(c) shows the TCSPC decay profile of perovskite 3, demonstrating average carrier lifetimes of 83.22 ns and 592.24 ns. It is to be noted that the significant differences in carrier lifetime across different perovskites can be attributed to bulk defects arising from variations in A-cation and halide compositions.[56–58] All the bi-exponential fitting parameters of the TCSPC decay analysis are tabulated in Table 2. Furthermore, the TCSPC decay profiles are fitted with the equation mentioned in Note 1 (SI) to quantify the recombination dynamics. The fitting parameters are tabulated in Table 3. The results indicate one order reduction in the SRH recombination constant (k_1) with the incorporation of Ion-Spiro HTL in all cases.

The absorption and photoluminescence (PL) spectra of perovskites 1, 2, and 3 are shown in Fig. S11. Optical analysis confirms that the band edge of the perovskite remained unchanged with the incorporation of different HTLs, although a slight increase in the overall absorbance with the ion-modulated spiro-MeOTAD HTL incorporated sample of perovskite 1 is observed. This effect is attributed to minor degradation of perovskite 1 with the regular spiro-MeOTAD HTL during the post-oxidation treatment. Illuminating the samples from the HTL/perovskite interface during PL analysis revealed a noticeable change in radiative intensities. Moreover, the optical analysis agrees well with the carrier lifetime and J–V

Table 2 Fitting parameters of the TCSPC carrier lifetime decay profile

Device	HTL	A1	A2	τ_1 (ns)	τ_2 (ns)	τ_{avg} (ns)
Perovskite 1	Control	0.56	0.13	39.8	431.7	318.79
	Ion-Spiro	0.41	0.34	58.3	647.5	589.76
Perovskite 2	Control	0.73	0.09	21.3	68.9	34.75
	Ion-Spiro	0.57	0.38	27.8	69.1	53.49
Perovskite 3	Control	0.53	0.34	20.1	102.7	83.22
	Ion-Spiro	0.15	0.61	39.36	601.15	592.24

Table 3 TCSPC fitting parameters of perovskite 1, 2, and 3 with the control and Ion-Spiro HTL

Sample	HTL	k_1 (S^{-1})	k_2 ($cm^3\ S^{-1}$)
Perovskite 1	Control	3×10^6	5×10^{-10}
	Ion-Spiro	9×10^5	2.5×10^{-10}
Perovskite 2	Control	1×10^7	2.5×10^{-10}
	Ion-Spiro	9.4×10^6	3×10^{-10}
Perovskite 3	Control	9×10^6	1×10^{-11}
	Ion-Spiro	6×10^5	3×10^{-11}

analysis. Further validation of the role of interfacial defects between the HTL and perovskite is performed through photoluminescence quantum yield (PLQY) analysis. The trends observed in TCSPC analyses were consistent with PLQY results. Perovskite 2 exhibited minimal PLQY differences between control and ion-modulated spiro-MeOTAD samples, with values of 0.46% and 0.55%, respectively (Fig. 3(b) inset). In contrast, perovskite 1 exhibited a significant improvement from 0.28% to 1.2% upon incorporating ion-modulated spiro-MeOTAD (Fig. 3(a) inset). Similarly, perovskite 3 displayed a PLQY increase from 0.31% to 3.9% (Fig. 3(c) inset). Fig. 3(d) illustrates the estimated quasi-Fermi level splitting (QFLS), quantified using eqn (1), for all three perovskite compositions with both control and ion-modulated spiro-MeOTAD HTLs. It is to be noted that the observed differences in PLQY are not directly reflected in the QFLS values, which can be attributed to the logarithmic correlation between the PLQY and QFLS, as described by eqn (1). Further details regarding the QFLS estimation from PLQY measurements with the used parameters J_G and $J_{0,rad}$ are provided in the SI, in Table S1 and Fig. S12, respectively.

The Shockley–Queisser equation for determining the radiative recombination density of free charges (J_{rad}) using the chemical potential per free electron–hole pair, given by μ or QFLS in the active materials, can be written as

$$J_{rad} = J_{0,rad} \cdot \exp \frac{\mu}{k_B T} \quad (1)$$

To gain deeper insight into whether the enhancement of the V_{OC} arises primarily from energy level alignment or from interfacial defects, we performed theoretical simulations for perovskite 1 by introducing band offsets between the absorber and the HTL in both the positive and negative directions, as illustrated in Fig. 4(a). The simulated $J-V$ characteristics indicate that variations in band offsets do not significantly influence V_{OC}, with only minor changes observed in the FF. In contrast, simulations performed with varying k_1 reveal a clear dependence of V_{OC} on k_1, as shown in Fig. 4(b). Additionally, we calculated the difference between the experimentally measured and analytically determined V_{OC}, as shown in Fig. 4(c). The analytical values of V_{OC} are derived from the recombination constants and J_{SC}, as detailed in Note 1 (SI). The close agreement between the analytical and experimental results confirms that interfacial effects in devices employing the control spiro-OMeTAD HTL play a dominant role in determining the V_{OC}. Notably, the small variation in FF observed between the control and Ion-Spiro-based devices can be attributed primarily to differences in series resistance, as demonstrated in Fig. 4(d).

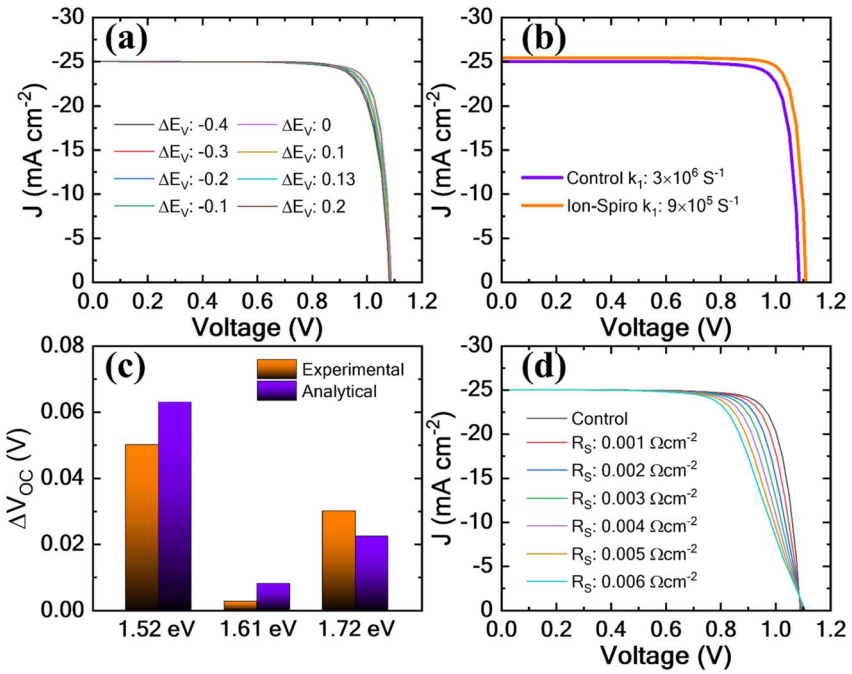

Fig. 4 Theoretical validation of the role of interface defects with Ion-Spiro-based devices. (a) Simulated $J-V$ characteristics of perovskite 1 with varying band offsets (both positive and negative) between the absorber and HTL, (b) effect of varying SRH recombination constant (k_1) on device performance, (c) comparison of open-circuit voltage (V_{OC}) differences for experimental measurements and analytical estimations for control and Ion-Spiro HTL-based devices, and (d) influence of varying fill factor (FF) in $J-V$ analysis under series resistance conditions.

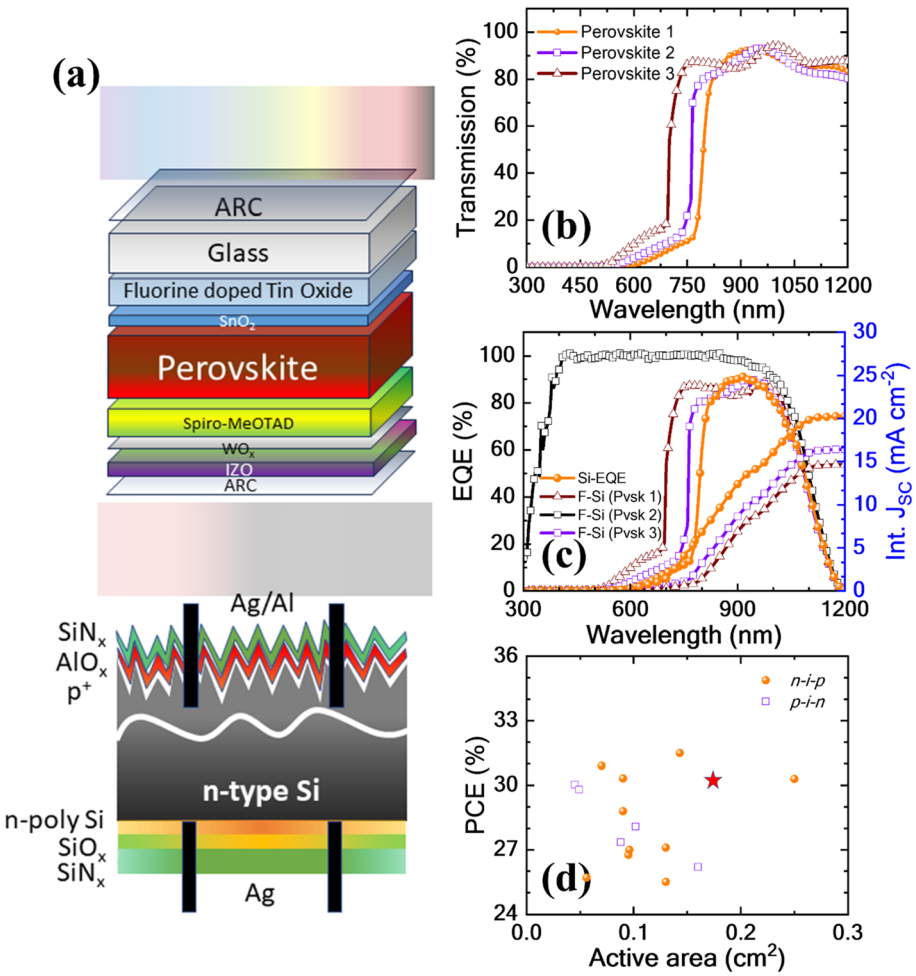

Fig. 5 Mechanically stacked 4T Si/perovskite tandem solar cells. (a) Schematic representation of the device stack of mechanically coupled 4T Si/perovskite tandem solar cells, (b) transmission spectra of the variable bandgap transparent PSCs, (c) EQE spectra of the standalone Si and perovskite filtered Si solar cells, and (d) comparison of literature reports of 4T tandem efficiency with this study with respect to the active area.

The optimized transparent PSCs with variable band gaps are coupled with a monocrystalline Si solar cell in a mechanically coupled 4T tandem configuration. Fig. 5(a) presents a schematic representation of the mechanically stacked 4T Si/perovskite tandem solar cells. In this configuration, n-type tunnel oxide passivated contact (n-TOPCon) Si solar cells are employed as the bottom absorbers. Sunlight is incident from the glass/FTO side of the perovskite top cells. Short-wavelength photons are absorbed by the PSCs, while long-wavelength photons are transmitted through the top PSCs and subsequently absorbed by the bottom Si cells. Fig. 5(b) illustrates the transmission spectra of the transparent PSCs with variable band gaps, while Fig. 5(c) shows the EQE spectrum of standalone Si solar cells, along with the perovskite filtered EQE spectra of Si solar cells and the corresponding integrated J_{SC}. The standalone PCE of the Si solar cells is 25.5%. However, after filtering through the top PSCs, the PCE of the n-TOPCon Si solar cells decreased to 8.9%, 10%, and 12.3% for perovskite configurations 1, 2, and 3, respectively. The filtered efficiency of the n-TOPCon Si solar cells is determined based on the transmission spectrum of the individual PSCs and the EQE of the Si solar cells. The simulated integrated photocurrent densities of the Si solar cells are found to be 14.67 mA cm^{-2}, 16.42 mA cm^{-2}, and 20.28 mA cm^{-2} after filtering through perovskites 1, 2, and 3, respectively. Consequently, upon adding the PCEs of the transparent PSCs to the filtered n-TOPCon Si solar cell performance, overall PCEs of 30.2%, 29.4%, and 28.4% are achieved for perovskite 1, 2, and 3, respectively. In all cases, the developed 4T Si/perovskite tandem solar cells are substantially more efficient than the standalone Si solar cells. The tandem cells show efficiency improvements of 18.4%, 15.2%, and 11.4% (over the standalone Si cells) when paired with perovskites 1, 2, and 3, respectively. Notably, the monocrystalline n-TOPCon Si solar cell-based tandem configuration exhibited a substantial PCE enhancement of ~18%, increasing from 25.5% to 30.2%. The PV performance metrics of all 4T tandem solar cells are summarized in Table 4. Fig. 5(d) compares the photovoltaic performance of the 4T Si/perovskite tandem solar cells from this study with reports in the literature based on the active area.[59–69] The results indicate that the observed PCE is well aligned with previously reported values and represents one of the highest

Table 4 4T Si/perovskite tandem PV performance

Device	J_{SC} (mA cm^{-2})	V_{OC} (V)	FF (%)	PCE (%)
Perovskite 1	25.39	1.13	73.7	21.3
Perovskite 2	23.70	1.13	72.5	19.4
Perovskite 3	19.60	1.19	68.7	16.1
Si stand alone	42.09	0.72	84.2	25.5
Perovskite 1-F-Si	14.67	0.72	84.2	8.9
Perovskite 2-F-Si	16.42	0.72	84.2	10
Perovskite 3-F-Si	20.28	0.72	84.2	12.3
4T (Si + Perovskite 1)	—	—	—	30.2
4T (Si + Perovskite 2)	—	—	—	29.4
4T (Si + Perovskite 3)	—	—	—	28.4

efficiencies among transparent PSCs when evaluated based on the active area.

The stability of transparent PSCs using both control and ion-modulated spiro-MeOTAD is evaluated under dark N_2 storage, continuous heating at 65 °C, continuous illumination, and MPPT conditions (Fig. S13). Across all tests, the ion-modulated spiro-MeOTAD devices showed marginally improved stability, corroborating reduced interfacial defects and improved robustness of the organic HTL.

Discussion

This study explores the substitution of conventional LiTFSI- and t-BP-doped spiro-MeOTAD with a post-oxidation-free, ion-modulated spiro-MeOTAD. Along with the post-oxidation free requirement, the presented approach enables precise tuning of the work function with reduced non-radiative recombination losses at the HTL/perovskite interface through TBMPTFSI salt doping. Tuning the bandgap of perovskite absorbers *via* halide composition primarily influences the VBM, owing to the strong contribution of halide p-orbitals. As a result, increasing the bandgap induces a progressive downward shift (towards deeper energy levels) of the VBM, a trend also confirmed by UPS analysis,[70] although some studies have suggested that a negative energy-band offset might hinder hole transport by creating an interfacial misalignment.[71,72] However, it is also proven that, in many cases, such conclusions likely arise from inaccuracies in determining the absolute energy levels rather than from an actual physical barrier.[71,72] Additionally, it is also well established that perovskite absorbers tend to self-adjust their interfacial energy levels, making them relatively insensitive to minor variations in the band offset with the HTL.[73]

In agreement with this, our experimental findings, supported by theoretical modelling, indicate that the observed band offset induces only negligible variations in voltage losses and FF. Instead, the variations in the V_{OC} are predominantly governed by interfacial recombination dynamics, in agreement with the classical findings of McGehee *et al.*, which demonstrated that the HOMO level of the HTL exerts minimal influence on the V_{OC} of PSCs.[55] These results collectively underscore that mitigating interfacial defect states, rather than optimizing energy level alignment, is critical, particularly when VBM shifts are introduced through bandgap tuning. In this context, the utilization of Ion-Spiro, a post-oxidation-free and compositionally stable HTL, represents a promising strategy for modulating the HOMO level while concurrently minimizing SRH non-radiative recombination losses. Importantly, this approach exhibits broad applicability: irrespective of whether the perovskite bandgap shifts toward higher or lower energies, Ion-Spiro facilitates the formation of a defect-suppressing and energetically favourable interface. Consequently, a pronounced reduction in interfacial recombination and an enhancement in the QFLS are achieved, as evidenced by the experimental results presented in Fig. 2, 3, and 4.

Therefore, the precise tuning of HTL-induced interfacial defects with bandgap-tunable perovskites is further extended to tandem solar cells. This study provides compelling evidence for the potential of highly efficient and stable tunable bandgap transparent PSCs for tandem applications. To evaluate this proposed strategy, three different band gaps are employed for incorporating ion-modulated spiro-MeOTAD. It was observed that perovskite 2, with a bandgap of 1.61 eV, exhibited minimal differences in both optical and PV performance due to near-ideal interfacial defects with the regular HTLs. However, deviations from this optimal bandgap either towards narrower bandgap perovskite 1 (1.52 eV) or wider bandgap perovskite 3 (1.72 eV) resulted in significant variations in optoelectronic properties, as evidenced in Fig. 2 and 3. Notably, upon introducing tuned TBMPTFSI-doped ion-modulated spiro-MeOTAD, a considerable enhancement in V_{OC} and FF in perovskite 1 and 3 is observed. Further optical investigations, supported by theoretical simulations, indicate that the reduction of interfacial defects, evidenced by lower SRH recombination constants, leads to enhanced device performance. Moreover, the optimized transparent PSCs are coupled with a monocrystalline n-TOPCon Si solar cell with a standalone efficiency of 25.5%, yielding a maximum PCE exceeding 30%. These findings underscore the critical role of band alignment in optimizing carrier dynamics and demonstrate the effectiveness of ion-modulated spiro-MeOTAD in mitigating interfacial defects. This is particularly significant for variable bandgap perovskite solar cells, enabling the achievement of higher PCEs.

Conclusions

This study demonstrates the efficacy of ion-modulated spiro-MeOTAD in replacing conventional LiTFSI- and t-BP-doped spiro-MeOTAD HTLs while eliminating post-oxidation requirements. The incorporation of TBMPTFSI salt enables a reduction in interfacial defects with tunable work function, leading to improved PV performance. The findings indicate that minimal variations in PV performance are observed for perovskite 2 (1.61 eV), as the conventional doped spiro-MeOTAD HTL is predominantly optimized for this bandgap. However, deviations from this bandgap on either side resulted in band misalignment, increased interfacial surface defects, and reduced PCE. Notably, the introduction of ion-modulated spiro-MeOTAD with an optimized work function significantly enhanced surface defect tolerance, thereby influencing carrier dynamics, resulting in improved 2–5% V_{OC} and 6–7% FF in

perovskite 1 and 3. Thus, Ion-Spiro offers an effective strategy to enhance surface defect tolerance, irrespective of the perovskite absorber's bandgap. Moreover, the successful integration of optimized transparent PSCs with a monocrystalline n-TOPCon Si solar cell achieved a tandem efficiency of 30.2%, representing an ~18% improvement. These results underscore the critical role of interfacial defect passivation with ion-modulated spiro-MeOTAD in advancing high-efficiency, stable PSCs for tandem applications, presenting a promising pathway for the next generation of photovoltaic technology.

Conflicts of interest

The authors declare no conflicts of interest.

Data availability

The experimental data are available from the corresponding authors upon reasonable request.

Supplementary information (SI): comprehensive details of the experimental methodologies and characterization protocols employed in this study. It further presents work function measurements, photovoltaic (PV) performance optimization, and device reliability. See DOI: https://doi.org/10.1039/d5el00175g.

Acknowledgements

The authors acknowledge MoE-India for the doctoral fellowship. This work is also partially supported by the DST-Solar Challenge Award (DST/ETC/CASE/RES/2023/02). DK also acknowledges Forbes Marshall's financial support for the Energy Science & Engineering chair professorship. The authors acknowledge Rory Back and Su Verma from Pilkington for providing the FTO substrates. The authors are also grateful to MNRE sponsored NCPRE and IIT Bombay for providing all the fabrication and characterization facilities.

References

1 J. Y. Kim, J. W. Lee, H. S. Jung, H. Shin and N. G. Park, *Chem. Rev.*, 2020, **120**(15), 7867–7918.
2 M. A. Green and A. W. Y. Ho-Baillie, *ACS Energy Lett.*, 2019, **4**(7), 1639–1644.
3 O. Grånäs, D. Vinichenko and E. Kaxiras, *Sci. Rep.*, 2016, **6**, 36108.
4 M. Degani, Q. An, M. Albaladejo-Siguan, Y. J. Hofstetter, C. Cho, F. Paulus, G. Grancini and Y. Vaynzof, *Sci. Adv.*, 2021, **7**, 7930.
5 S. Bitton and N. Tessler, *J. Mater. Chem. C*, 2021, **9**, 1888–1894.
6 A. Tara, A. Paul, A. Singha, S. Gohri, J. Madan, R. Pandey, P. Kumar, I. Hossain and S. Bhattarai, *J. Nanopart. Res.*, 2024, **26**, 278.
7 S. E. Sofia, H. Wang, A. Bruno, J. L. Cruz-Campa, T. Buonassisi and I. M. Peters, *Sustainable Energy Fuels*, 2020, **4**, 852–862.
8 L. McGovern, E. C. Garnett, S. Veenstra and B. van der Zwaan, *Sustainable Energy Fuels*, 2023, **7**, 5259–5270.
9 Y. Vaynzof, D. Kabra, L. Zhao, P. K. H. Ho, A. T. S. Wee and R. H. Friend, *Appl. Phys. Lett.*, 2010, **97**, 156.
10 J. T. W. Wang, Z. Wang, S. Pathak, W. Zhang, D. W. Dequilettes, F. Wisnivesky-Rocca-Rivarola, J. Huang, P. K. Nayak, J. B. Patel, H. A. Mohd Yusof, Y. Vaynzof, R. Zhu, I. Ramirez, J. Zhang, C. Ducati, C. Grovenor, M. B. Johnston, D. S. Ginger, R. J. Nicholas and H. J. Snaith, *Energy Environ. Sci.*, 2016, **9**, 2892–2901.
11 G. J. A. H. Wetzelaer, M. Scheepers, A. M. Sempere, C. Momblona, J. Ávila and H. J. Bolink, *Adv. Mater.*, 2015, **27**, 1837–1841.
12 T. C.-J. Yang, T. Kang, M. Fitzsimmons, G. Vega, Y. Lu, L. Rosado, A. Jiménez-Solano, L. Pan, S. J. Zelewski, J. Ferrer Orri, Y.-H. Chiang, D. Guo, Z. Y. Ooi, Y. Han, W. Xu, B. Roose, C. Ducati, S. Carretero Palacios, M. Anaya and S. D. Stranks, *EES Sol.*, 2025, **1**, 41–55.
13 E. Ugur, A. A. Said, P. Dally, S. Zhang, C. E. Petoukhoff, D. Rosas-Villalva, S. Zhumagali, B. K. Yildirim, A. Razzaq, S. Sarwade, A. Yazmaciyan, D. Baran, F. Laquai, C. Deger, I. Yavuz, T. G. Allen, E. Aydin and S. De Wolf, *Science*, 1979, **385**, 533–538.
14 A. Paul, A. Singha, K. Hossain, S. Gupta, M. Misra, S. Mallick, A. H. Munshi and D. Kabra, *ACS Energy Lett.*, 2024, **9**, 3019–3026.
15 S. Chozas-Barrientos, A. Paliwal, F. Ventosinos, C. Roldán-Carmona, L. Gil-Escrig, V. Held, P. Carroy, D. Muñoz and H. J. Bolink, *ACS Energy Lett.*, 2025, 1733–1740.
16 S. Mariotti, E. Köhnen, F. Scheler, K. Sveinbjörnsson, L. Zimmermann, M. Piot, F. Yang, B. Li, J. Warby, A. Musiienko, D. Menzel, F. Lang, S. Keßler, I. Levine, D. Mantione, A. Al-Ashouri, M. S. Härtel, K. Xu, A. Cruz, J. Kurpiers, P. Wagner, H. Köbler, J. Li, A. Magomedov, D. Mecerreyes, E. Unger, A. Abate, M. Stolterfoht, B. Stannowski, R. Schlatmann, L. Korte and S. Albrecht, *Science*, 2023, **381**, 63–69.
17 Longi, 34.6%! Record-breaker LONGi Once Again Sets a New World Efficiency for Silicon-perovskite Tandem Solar Cells.
18 D. Chojniak, M. Steiner, S. K. Reichmuth, A. Schmid, G. Siefer, S. Hooper, D. Bushnell, D. Kirk, C. Case and S. W. Glunz, *EES Sol.*, 2025, **1**, 66–77.
19 Longi, 34.85%! LONGi Breaks World Record for Crystalline Silicon-Perovskite Tandem Solar Cell Efficiency Again.
20 E. Raza and Z. Ahmad, *Energy Reports*, 2022, **8**, 5820–5851.
21 A. Singha, A. Paul, S. Koul, V. Sharma, S. Mallick, K. R. Balasubramaniam and D. Kabra, *Sol. RRL*, 2023, **7**(12), 2300117.
22 L. A. Zafoschnig, S. Nold and J. C. Goldschmidt, *IEEE J. Photovoltaics*, 2020, **10**, 1632–1641.
23 S. E. Sofia, H. Wang, A. Bruno, J. L. Cruz-Campa, T. Buonassisi and I. M. Peters, *Sustainable Energy Fuels*, 2020, **4**, 852–862.
24 W. Yang, H. Long, X. Sha, J. Sun, Y. Zhao, C. Guo, X. Peng, C. Shou, X. Yang, J. Sheng, Z. Yang, B. Yan and J. Ye, *Adv. Funct. Mater.*, 2022, **32**(12), 2110698.

25 P. Caprioglio, J. A. Smith, R. D. J. Oliver, A. Dasgupta, S. Choudhary, M. D. Farrar, A. J. Ramadan, Y. H. Lin, M. G. Christoforo, J. M. Ball, J. Diekmann, J. Thiesbrummel, K. A. Zaininger, X. Shen, M. B. Johnston, D. Neher, M. Stolterfoht and H. J. Snaith, *Nat. Commun.*, 2023, **14**, 932.
26 Q. Xue, R. Xia, C. J. Brabec and H. L. Yip, *Energy Environ. Sci.*, 2018, **11**, 1688–1709.
27 C. D. Bailie, M. G. Christoforo, J. P. Mailoa, A. R. Bowring, E. L. Unger, W. H. Nguyen, J. Burschka, N. Pellet, J. Z. Lee, M. Grätzel, R. Noufi, T. Buonassisi, A. Salleo and M. D. McGehee, *Energy Environ. Sci.*, 2015, **8**, 956–963.
28 T. Lemercier, L. Perrin, E. Planès, S. Berson and L. Flandin, *Energies*, 2020, **13**(15), 3794.
29 L. Lin, T. W. Jones, T. C. J. Yang, N. W. Duffy, J. Li, L. Zhao, B. Chi, X. Wang and G. J. Wilson, *Adv. Funct. Mater.*, 2021, **31**(5), 2008300.
30 R. H. Ahangharnejhad, J. D. Friedl, A. B. Phillips and M. J. Heben, *Sol. Energy Mater. Sol. Cells*, 2021, **225**, 111015.
31 D. Ompong and J. Singh, *Org. Electron.*, 2018, **63**, 104–108.
32 N. K. Kumawat, M. N. Tripathi, U. Waghmare and D. Kabra, *J. Phys. Chem. A*, 2016, **120**, 3917–3923.
33 L. Wang, Z. Yan, J. Qiu, J. Wu, C. Zhen, K. Tai, X. Jiang and S. Yang, *Nano Energy*, 2021, **90**(Part A), 106537.
34 M. Jaysankar, B. A. L. Raul, J. Bastos, C. Burgess, C. Weijtens, M. Creatore, T. Aernouts, Y. Kuang, R. Gehlhaar, A. Hadipour and J. Poortmans, *ACS Energy Lett.*, 2019, **4**, 259–264.
35 Z. Zhao, W. Liu, T. Kong, Y. Liu, W. Chen, P. Gao and D. Bi, *Adv. Funct. Mater.*, 2025, **35**(16), 2419393.
36 Z. Wei, Q. Zhou, X. Niu, S. Liu, Z. Dong, H. Liang, J. Chen, Z. Shi, X. Wang, Z. Jia, X. Guo, R. Guo, X. Meng, Y. D. Wang, N. Li, Z. Xu, Z. Li, A. G. Aberle, X. Yin and Y. Hou, *Energy Environ. Sci.*, 2025, **18**, 1847–1855.
37 Y. Zhao, C. Wang, T. Ma, L. Zhou, Z. Wu, H. Wang, C. Chen, Z. Yu, W. Sun, A. Wang, H. Huang, B. Zou, D. Zhao and X. Li, *Energy Environ. Sci.*, 2023, **16**, 2080–2089.
38 H. Zhu, S. Teale, M. N. Lintangpradipto, S. Mahesh, B. Chen, M. D. McGehee, E. H. Sargent and O. M. Bakr, *Nat. Rev. Mater.*, 2023, **8**, 569–586.
39 T. A. Chowdhury, M. A. Bin Zafar, M. Sajjad-Ul Islam, M. Shahinuzzaman, M. A. Islam and M. U. Khandaker, *RSC Adv.*, 2023, **13**, 1787–1810.
40 A. Singha, A. Paul, N. Gaur, H. S. Bilkhu, A. Arya, V. Bhalerao, S. Mallick, K. R. Balasubramaniam and D. Kabra, *Small*, 2025, **20**, 2502659.
41 A. K. Jena, Y. Numata, M. Ikegami and T. Miyasaka, *J. Mater. Chem. A*, 2018, **6**, 2219–2230.
42 S. Y. Jeong, H. S. Kim and N. G. Park, *ACS Appl. Mater. Interfaces*, 2022, **14**(30), 34220–34227.
43 G. Ren, W. Han, Y. Deng, W. Wu, Z. Li, J. Guo, H. Bao, C. Liu and W. Guo, *J. Mater. Chem. A*, 2021, **9**, 4589–4625.
44 S. Wang, Z. Huang, X. Wang, Y. Li, M. Günther, S. Valenzuela, P. Parikh, A. Cabreros, W. Xiong and Y. S. Meng, *J. Am. Chem. Soc.*, 2018, **140**, 16720–16730.
45 S. G. Kim, T. H. Le, T. de Monfreid, F. Goubard, T. T. Bui and N. G. Park, *Adv. Mater.*, 2021, **33**(12), 2007431.
46 A. K. Jena, Y. Numata, M. Ikegami and T. Miyasaka, *J. Mater. Chem. A*, 2018, **6**, 2219–2230.
47 S. Toikkonen, G. K. Grandhi, S. Wang, B. Baydin, B. Al-Anesi, L. K. Jagadamma and P. Vivo, *Adv. Devices Instrum.*, 2024, **5**, 0048.
48 T. Zhang, F. Wang, H.-B. Kim, I.-W. Choi, C. Wang, E. Cho, R. Konefal, Y. Puttisong, K. Terado, L. Kobera, M. Chen, M. Yang, S. Bai, B. Yang, J. Suo, S.-C. Yang, X. Liu, F. Fu, H. Yoshida, W. M. Chen, J. Brus, V. Coropceanu, A. Hagfeldt, J.-L. Brédas, M. Fahlman, D. Suk Kim, Z. Hu and F. Gao, *Science*, 2022, **377**, 495–501.
49 M. Saliba, T. Matsui, J. Y. Seo, K. Domanski, J. P. Correa-Baena, M. K. Nazeeruddin, S. M. Zakeeruddin, W. Tress, A. Abate, A. Hagfeldt and M. Grätzel, *Energy Environ. Sci.*, 2016, **9**, 1989–1997.
50 L. Wang, Z. Yan, J. Qiu, J. Wu, C. Zhen, K. Tai, X. Jiang and S. Yang, *Nano Energy*, 2021, **90**(Part A), 106537.
51 Q. Jiang, J. Tong, Y. Xian, R. A. Kerner, S. P. Dunfield, C. Xiao, R. A. Scheidt, D. Kuciauskas, X. Wang, M. P. Hautzinger, R. Tirawat, M. C. Beard, D. P. Fenning, J. J. Berry, B. W. Larson, Y. Yan and K. Zhu, *Nature*, 2022, **611**, 278–283.
52 A. Paul, A. Singha, S. Koul, S. Nayak, N. Gaur, S. Mallick, B. Kavaipatti and D. Kabra, *ACS Appl. Mater. Interfaces*, 2024, **16**, 60258–60267.
53 A. Singha, A. Paul, S. Manna, C. K. Sahoo, V. Kumar, A. Kottantharayil, S. Mallick, K. R. Balasubramaniam and D. Kabra, *EES Sol.*, 2025, **1**, 1160–1172.
54 A. Paul, A. Singha, V. Sharma, S. Mallick, K. R. Balasubramaniam and D. Kabra, *J. Phys. D Appl. Phys.*, 2025, **58**, 415107.
55 R. A. Belisle, P. Jain, R. Prasanna, T. Leijtens and M. D. McGehee, *ACS Energy Lett.*, 2016, **1**, 556–560.
56 A. Solanki, P. Yadav, S. H. Turren-Cruz, S. S. Lim, M. Saliba and T. C. Sum, *Nano Energy*, 2019, **58**, 604–611.
57 W. Rehman, R. L. Milot, G. E. Eperon, C. Wehrenfennig, J. L. Boland, H. J. Snaith, M. B. Johnston and L. M. Herz, *Adv. Mater.*, 2015, **27**, 7938–7944.
58 P. Srivastava, R. Kumar and M. Bag, *J. Phys. Chem. C*, 2021, **125**, 211–222.
59 Y. Zhang, L. Zhou and C. Zhang, *Energies*, 2024, **17**(8), 1833.
60 Y. Yao, P. Hang, B. Li, Z. Hu, C. Kan, J. Xie, Y. Wang, Y. Zhang, D. Yang and X. Yu, *Small*, 2022, **18**(38), 2203319.
61 J. Xu, C. C. Boyd, Z. J. Yu, A. F. Palmstrom, D. J. Witter, B. W. Larson, R. M. France, J. Werner, S. P. Harvey, E. J. Wolf, W. Weigand, S. Manzoor, M. F. A M van Hest, J. M. Luther, Z. C. Holman and M. D. McGehee, *Science*, 2020, **367**(6482), 1097–1104.
62 P. Löper, S. J. Moon, S. Martín De Nicolas, B. Niesen, M. Ledinsky, S. Nicolay, J. Bailat, J. H. Yum, S. De Wolf and C. Ballif, *Phys. Chem. Chem. Phys.*, 2015, **17**, 1619–1629.
63 M. Schultes, T. Helder, E. Ahlswede, M. F. Aygüler, P. Jackson, S. Paetel, J. A. Schwenzer, I. M. Hossain, U. W. Paetzold and M. Powalla, *ACS Appl. Energy Mater.*, 2019, **2**, 7823–7831.
64 B. Chen, S. W. Baek, Y. Hou, E. Aydin, M. De Bastiani, B. Scheffel, A. Proppe, Z. Huang, M. Wei, Y. K. Wang, E. H. Jung, T. G. Allen, E. Van Kerschaver, F. P. García de

Arquer, M. I. Saidaminov, S. Hoogland, S. De Wolf and E. H. Sargent, *Nat. Commun.*, 2020, **11**, 1257.
65 Z. Wang, X. Zhu, S. Zuo, M. Chen, C. Zhang, C. Wang, X. Ren, Z. Yang, Z. Liu, X. Xu, Q. Chang, S. Yang, F. Meng, Z. Liu, N. Yuan, J. Ding, S. Liu and D. Yang, *Adv. Funct. Mater.*, 2020, **30**(4), 1908298.
66 Z. Fang, B. Deng, Y. Jin, L. Yang, L. Chen, Y. Zhong, H. Feng, Y. Yin, K. Liu, Y. Li, J. Zhang, J. Huang, Q. Zeng, H. Wang, X. Yang, J. Yang, C. Tian, L. Xie, Z. Wei and X. Xu, *Nat. Commun.*, 2024, **15**, 10554.
67 Z. Liu, C. Zhu, H. Luo, W. Kong, X. Luo, J. Wu, C. Ding, Y. Chen, Y. Wang, J. Wen, Y. Gao and H. Tan, *Adv. Energy Mater.*, 2023, **13**(2), 2203230.
68 L. Du, C. Li, Y. Jiang, F. Cao, C. Jia, Z. Wan, R. Meng, J. Shi, C. Xiao, Z. Liu and Z. Li, *J. Energy Chem.*, 2025, **102**, 189–196.
69 S. Ašmontas, J. Gradauskas, A. Grigucevičienė, K. Leinartas, A. Lučun, M. Mujahid, K. Petrauskas, A. Selskis, A. Sužiedėlis, A. Šilėnas and E. Širmulis, *Ukr. J. Phys. Opt.*, 2022, **23**(4), 193–200.
70 M. Wuttig, C. F. Schön, M. Schumacher, J. Robertson, P. Golub, E. Bousquet, C. Gatti and J. Y. Raty, *Adv. Funct. Mater.*, 2022, **32**(2), 2110166.
71 F. M. Rombach, S. A. Haque and T. J. Macdonald, *Energy Environ. Sci.*, 2021, **14**, 5161–5190.
72 P. Schulz, D. Cahen and A. Kahn, *Chem. Rev.*, 2019, **119**(5), 3349–3417.
73 C. Eames, J. M. Frost, P. R. F. Barnes, B. C. O'Regan, A. Walsh and M. S. Islam, *Nat. Commun.*, 2015, **6**, 7497.